Multi-Winding Configuration Optimization of Multi-Output Planar Transformers in GaN Active Forward Converters for Satellite Applications

Zhiliang Zhang, *Senior Member, IEEE*, Binghui He, Dong-Dong Hu, Xiaoyong Ren, *Member, IEEE*, and Qianhong Chen, *Member, IEEE*

***Abstract*—It is a serious challenge to find the optimal winding configuration that realizes minimum leakage inductance of multi-output multi-winding planar transformers due to the complex coupling relationship. The proposed idea is to build the mathematical model of leakage magnetic field energy and screen out all possible winding configurations to solve the minimum value with MATLAB programming. Then, only limited potential winding configurations need to be three-dimensionally simulated in Maxwell. By analyzing the inductance matrix, the leakage inductance of multi-winding planar transformers is solved. A full gallium nitride (GaN) active clamp forward converter with self-driven synchronous rectifiers (SRs) is presented with complete mode analysis. It is noted that the proposed active clamp technology uses the auxiliary winding with the nonfloating GaN switch compared to the conventional high-side clamping circuit, which is important for the satellite applications. The GaN drive chips for high reliable gate voltage are combined with self-driving. Considering the leakage inductance in each winding and junction capacitance of the GaN high electron mobility transistors, the oscillation frequency and amplitude over the switches are modeled quantitatively, which is important to minimize powertrain loop at MHz. The explanation of the root cause of the voltage spike in the converter is also presented. A prototype with 1 MHz, 100 V input, 5 V/6 A and ±12 V/0.83 A outputs was built to verify the proposed techniques.**

***Index Terms*—Active clamp forward (ACF) converter, enhancement mode gallium nitride (eGaN) high electron mobility transistor (HEMT), finite element analysis (FEA), multi-winding planar transformer, synchronous rectification.**

NOMENCLATURE

n_1, n_2	Turns of primary winding and auxiliary winding.
D	Duty ratio of control HEMT Q_1.

Manuscript received March 20, 2018; revised June 17, 2018; accepted July 20, 2018. Date of publication July 31, 2018; date of current version March 29, 2019. This work was supported in part by the Natural Science Foundation of China under Grant 51722702, in part by the Outstanding Youth Fund of Jiangsu Province under Grant BK20160036, and in part by Fok Ying-Tong Education Foundation of China under Grant 151059. Recommended for publication by Associate Editor W. Huang. *(Corresponding author: Zhiliang Zhang.)*

Z. Zhang, B. He, X. Ren, and Q. Chen are with the Aero-Power Sci-Tech Center, Nanjing University of Aeronautics and Astronautics, Nanjing 211106, China (e-mail:

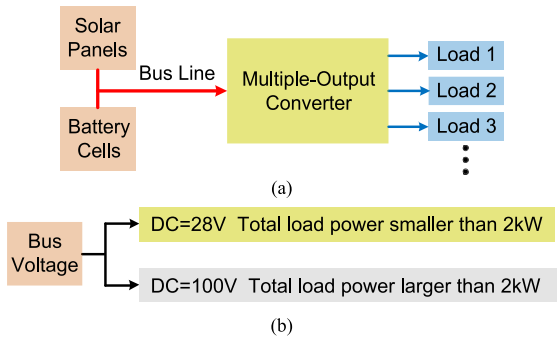

Fig. 1. Basic structure and bus voltage levels of the power supply system in satellites. (a) Basic structure of the satellite power supply system. (b) Bus voltage levels of the satellite power supply system.

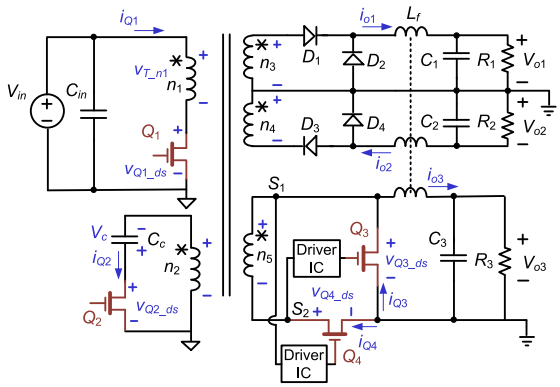

Fig. 2. GaN synchronous ACF multiple-output converter.

the total load power demand will increase in the future. When the total load power is above 2 kW, the bus voltage needs to increase to 100 V [6]–[8]. This bus voltage level is the trend in the power supply system of satellites, which reduces the power loss and weight of the transmission line and power system significantly.

The active clamp technique [9] is extensively used in multiple-output converters. Normally, the active clamp forward (ACF) converters [10], [11] are classified into the high-side clamping and the low-side clamping. The self-driven synchronous rectifier (SR) technique [12] is usually adopted in low-voltage and high-current output channels. At present, the typical switching frequency of the multiple-output converters is about 200–400 kHz and the MOSFETs are used. In order to shrink the size and weight of the passive components and further improve the power density, increasing the switching frequency to MHz range is an effective way [13]. However, this may result in higher frequency-dependent loss such as the switching loss, gate drive loss, magnetic loss, ac winding loss, and so on.

New generation of power device enhancement mode gallium nitride (eGaN) high electron mobility transistors (HEMTs) can improve high-frequency performance of multiple-output converters significantly [14]. Compared to the silicon MOSFETs with the similar voltage and current rating, the eGaN HEMTs have many advantages such as lower gate charge, faster switching speed, and smaller package with much reduced parasitics. These advantages make the eGaN HEMTs more suitable to MHz dc–dc converters [15]–[17]. Particularly, as to the satellite power converters, the eGaN HEMTs can help to improve the reliability against the radiation in space application. Nevertheless, special attention has to be paid when applying the eGaN HEMTs. One thing is that the eGaN HEMTs have no body diodes. When the eGaN HEMTs are reversely conducting, the reverse current has to travel via the device by the reverse conduction mechanism. Due to high reverse conduction voltage, the reverse conduction loss becomes severe at MHz switching frequency. Therefore, it is important to minimize the reverse conduction time when the eGaN HEMTs operate as the SRs in MHz converters. More importantly, the gate drive voltage has to be restricted less than 6 V. Once the drive voltage exceeds 6 V, the eGaN HEMTs can be damaged, which makes the self-driving of the SRs challenging.

At the MHz switching frequency, the conventional wire-wound transformers [16] that have large leakage inductance and high altitude may not be suitable anymore. The planar transformers offer good consistency, low altitude [19], low parasitic parameters [19]–[21], and high repeatability. These advantages make the planar transformers [22] gradually become a critical component of high-frequency (HF) converters. In the optimization process of a planar transformer, the leakage inductance is the key point. Lower leakage inductances [23], [24] produce lower voltage spikes over the fast speeding switches. For two-winding planar transformers, the leakage inductances in the primary and secondary winding can be conveniently optimized by calculating the leakage magnetic field energy [25]. The leakage magnetic field energy is related to magneto motive force (MMF) [26], [27]. Due to the simple structure and limited winding layers, the optimal winding configuration with minimum leakage inductance can be found by interleaving windings intuitively. The typical result of winding optimization is usually a symmetrical interleaving structure [28]–[30]. However, this method is not suitable to multi-winding planar transformers straightforward. Due to high complexity of multi-output multi-winding configuration, all the leakage magnetic energy is coupled entirely. Therefore, it is difficult to calculate the leakage magnetic field energy of particular winding and related leakage inductance theoretically.

The objective of this paper is to propose an optimization method to identify the optimal structure for HF multi-winding planar transformers. Compared with the existing literature, this optimization combines numerical calculation and finite element analysis (FEA) simulation and is suitable to HF multi-winding planar transformers. A new active clamp technology using the auxiliary winding with the nonfloating GaN switch is proposed.

II. Synchronous Active Clamp Forward Converter

Fig. 2 shows the schematic of the ACF converter. Table I lists the specifications. Compared with the multiple-output forward converter [10], the duty ratio can exceed 50% and bidirectional magnetization can be realized in the converter.

Conventional high-side clamping requires the clamping circuit paralleled with the primary winding. Since the clamp branch is located on the high side, it needs a floating driver circuit.

TABLE I
CONVERTER SPECIFICATIONS

	Voltage (V)	Current (A)	Power (W)
Input	90~110	-	-
Output 1	+12	0.83 (low current)	10
Output 2	-12	0.83 (low current)	10
Output 3 (Main output)	5	6 (high current)	30

For satellite applications, the driver circuit should be simple and reliable. Since the floating driver circuit is complicated and unreliable, it is hardly applicable. The conventional low-side clamping requires the clamping circuit paralleled with the main switch and needs a p-channel switch. In Fig. 2, compared to the conventional high-side clamping circuit, the converter uses an auxiliary winding to implement the active clamp. The auxiliary circuit consists of a clamping switch and a clamping capacitor. The advantage of the proposed active clamp technology is that the main and clamping switches are driven conveniently and reliably without the floating driver circuits, which is important for satellite applications.

Considering the main output is 5 V/6 A, the self-driven SR is adopted to reduce the conduction loss. Compared with the conventional self-driven MOSFET SR, the eGaN HEMTs need extra driver IC to realize the SR. The reason is that the drive signals obtained from the transformer winding exceed the maximum gate voltage rating of eGaN HEMTs. To guarantee the safety drive voltage, a drive chip is adopted. The other two output channels only need to provide low output current, so the Schottky diodes are used. All the active switches in this converter are eGaN HEMTs and the switching frequency is targeted as 1 MHz.

III. DESIGN PROBLEMS OF A PLANAR MULTI-WINDING TRANSFORMER

To achieve high power density, the multiple-output planar transformer has been adopted in the ACF converter. A general method is to analyze the MMF distribution [16], [24] of windings in the window and calculate the leakage magnetic field energy of the transformer theoretically. According to (1), the energy stored in the leakage inductance is equal to the leakage magnetic field energy. By calculating the leakage magnetic field energy, the theoretical leakage inductance value can be solved conveniently

$$E_{\text{energy}} = \frac{1}{2}\int_{\substack{\text{window}\\ \text{area}}} BHdV = \frac{1}{2}L_{lk}I_P^2 \tag{1}$$

where L_{lk} is the leakage inductance in the primary side, I_p is the current of the primary winding, B is the magnetic induction intensity in the window, and H is the magnetic field strength in the window.

This method is verified to be effective in design and optimization of a two-winding planar transformer. Fig. 3 shows the diagram of a two-winding transformer. Considering the construction of the two-winding transformer is simple, it only needs

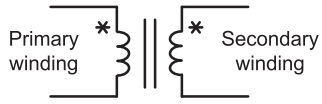

Fig. 3. Two-winding transformer.

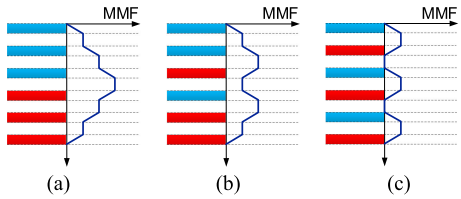

Fig. 4. (a) Noninterleaving structure. (b) Part-interleaving structure. (c) Interleaving structure.

to compare a few configurations that include the noninterleaving structure, part-interleaving structure, and interleaving structure to find the optimal structure [27]. Fig. 4 shows the MMF distribution of three possible winding configurations. The blue rectangle represents the primary winding and the red rectangle represents secondary winding. Normally, the interleaving structure has the smallest leakage inductance and this winding structure is proved to be the optimal winding configuration. The capacitive coupling between the primary winding and secondary winding normally increases with interleaved windings since the overlap area of windings is increased. The leakage inductance is decreased and the parasitic capacitance is increased.

As for the multiple-output converters, many practical factors need to be considered compared with the two-winding transformer. The main challenge of the ACF multiple-output converter is the design and optimization of the planar transformer with MHz. In the multiple-winding planar transformer, there are usually three or four windings and even more. Due to different output voltage and power, the turns and current of these secondary windings are different. There are tens of thousands of possible winding configurations that exist. The magnetic field and coupling relationship of a multiple-output transformer is more complex than a two-winding transformer. It is difficult to interleave one primary winding and several secondary windings manually to find the optimal arrangement compared with a simple two-winding transformer.

The reduction priority of the leakage inductance in the multi-windings is different. There are two criteria for selecting the optimal structure of the multi-winding planar transformer as 1) the first priority is that the total leakage magnetic field energy should be controlled within a low range to ensure that the leakage inductance of all windings is within an acceptable range; 2) the second priority is that the leakage inductance in the 5 V output channel should be as low as possible, since the 5 V output channel has low output voltage and high output current. The driving signals of the SRs are from the transformer winding. If the leakage inductance of this winding is large, the oscillations of driving signals are serious. These severe oscillations may result in false turn-ON of SRs. To ensure the SRs operate efficiently,

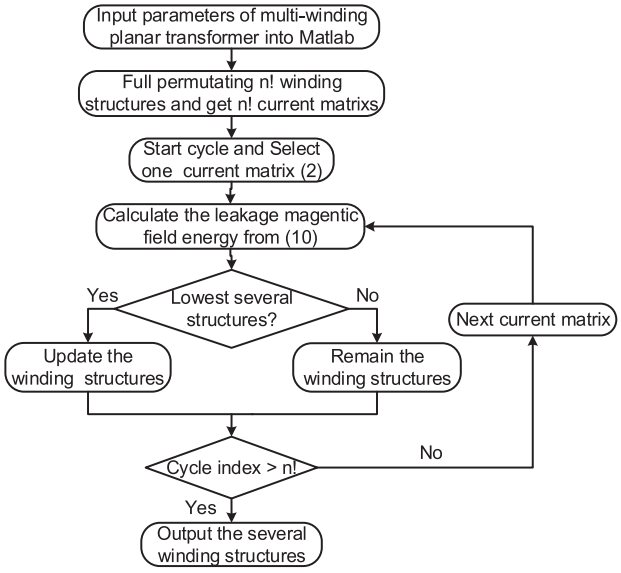

Fig. 5. Flowchart of numerical analysis.

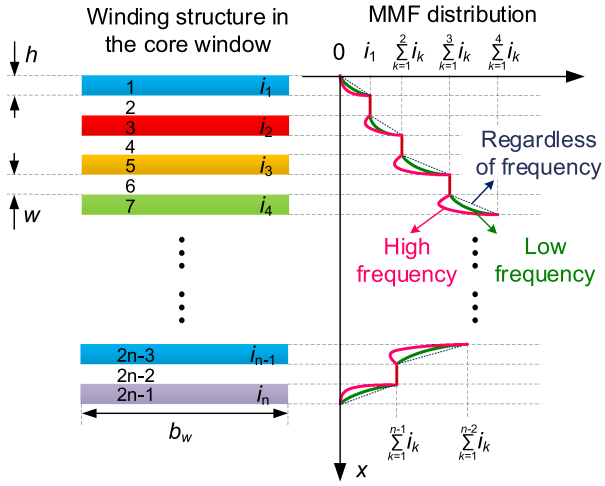

Fig. 6. MMF distribution of the winding structure.

the leakage inductance in this channel should be should be as low as possible. Therefore, the aim of optimization is to screen out potential structures that have low leakage magnetic field energy, and then find the optimal structure that has low leakage inductance in primary winding and main power winding from those possible configurations.

IV. Proposed Optimization Method of Multi-Winding Planar Transformers

A. Numerical Analysis Step

Fig. 5 shows the flowchart of the proposed numerical analysis. The parameters of a multiple-output planar transformer are input into a MATLAB program. The current in each layer i, the copper thickness h, the interlayer distance w, the width of magnetic core window b_W, and total layers n should be input into MATLAB. Then, through full permuting all n layers, $n!$ winding structures that correspond to $n!$ current matrixes are obtained. One of the matrixes is given as follows:

$$I = [i_1, i_2, i_3 \ldots i_n]. \tag{2}$$

In the hardware circuit, the currents have different values and directions. All the elements in matrix I depend on the particular winding structures. Due to the complex coupling relationship between the windings, (1) used in the simply two-winding transformers cannot be applied to the multiple-winding structure directly. However, the magnitude of the leakage magnetic field energy still reveals the magnitude of the leakage inductance. The number of layers in the multi-winding planar transformer is large. The total amount of possible configurations becomes large as well. The calculation cannot be finished manually. With MATLAB programming, a large number of cases that have high leakage magnetic energy can be filtered out. By doing this, the number of cases can be reduced to few options. This procedure can improve the screening efficiency and save a lot of design effort.

Fig. 6 shows the MMF distribution of a winding structure. The left part is the winding structure in the core window and the right part is the MMF distribution. h denotes the copper thickness. w denotes the interlayer distance. i denotes the current in each layer. b_W denotes the width of the magnetic core window. The total number of layers is n. It should be emphasized that the winding structure in Fig. 6 is only used to illustrate the calculation of total leakage magnetic field energy. In practical applications, the winding structure and parameter are not the same. There are some important points that can be summarized as follows.

1) The nth layer current i_n is defined as the total current in that layer. In the case with several turns in one layer, the current in each turn should be summed together. Besides, for the convenience of calculation, it is assumed that the magnetic field intensity is constant in the horizontal direction.
2) The nth layer current i_n can be either positive or negative. In other words, the current directions of the primary winding and secondary winding are opposite, which is corresponding to the positive and negative values of the current. Different interleaved winding arrangements correspond to different current matrixes and different MMF distributions. Once the winding structure is determined, the current matrix is determined by assuming that the direction out of the paper is positive while the direction into the paper is negative.
3) Due to the eddy current, which is caused by proximity effect and skin effect in HF situation, the load current is close to the surface of the conductor. This phenomenon results in the inhomogeneous distribution of magnetic field strength. The MMF distribution of the winding structure is different as well, which may reduce the total leakage magnetic field energy [31]. The different lines in Fig. 6 indicate the effect of higher frequencies on the MMF distribution.

By splitting the core window into $2n-1$ fractions, as shown in Fig. 6, the leakage magnetic field energy of each fraction is

$$E_{\text{leakage}} = \frac{1}{2}\int_V BHdV = \frac{\mu_0}{2}\int_V H^2 dV \tag{3}$$

where V denotes the volume of each fraction. Assuming the magnetic field intensity is constant in the horizontal direction, the expression of the magnetic field strength in the nth odd section of the window area is (4) shown at the bottom of this page, where

$$\gamma = \frac{1+j}{\delta} = (1+j)\sqrt{\pi f \mu_0 \sigma}. \tag{5}$$

In (5), δ denotes the skin depth and σ denotes the electrical conductivity of copper. Based on (3) and (4), the leakage magnetic field energy in the nth odd fraction is derived, as shown in (8) at the bottom of this page.

According to the ampere circuital theorem, the expression of the magnetic field strength in the nth even fraction of the window area is

$$H(x) = \frac{i_1 + i_2 + \cdots + i_n}{b_w} \quad (h < x \le h + w). \tag{6}$$

The leakage magnetic field energy in the nth even fraction is calculated as

$$E_{le} = \frac{1}{2}\int_V BHdV = \frac{\mu_0}{2}\int_V H^2 dV = \frac{\mu_0 b_w l_w}{2}\int_h^{h+w} H(x)^2 dx$$
$$= \frac{\mu_0 l_w w}{2b_w}(i_1 + i_2 + \cdots + i_n)^2. \tag{7}$$

Then, the leakage magnetic energy in each fraction can be calculated similarly, as shown in (9) at the bottom of this page. Therefore, the total leakage magnetic field energy is calculated by adding up all the values in (9), which is shown in (10) at the bottom of this page.

According to (10), once the winding structure is determined the total leakage magnetic field energy can be calculated quantitatively. By screening out all the possible winding structures and comparing calculation results, several potential winding structures that have low leakage magnetic field energy can be obtained conveniently.

B. FEA Analysis Step

In the FEA analysis step, the models for the selected cases that have just been screened out in the numerical analysis are established. With the help of Maxwell, the self-inductance and mutual-inductance matrix and the ac resistance of all the cases can be obtained. Then, the leakage inductance in each winding can be calculated numerically. All the cases are sorted by the

$$H(x) = \frac{[(i_1 + i_2 + \cdots + i_n)\sinh(\gamma h) + (i_1 + i_2 + \cdots + i_{n-1})\sinh(\gamma h - \gamma x)]}{b_w \sinh(\gamma h)} (0 \le x \le h) \tag{4}$$

$$E_{lo} = \frac{1}{2}\int_V BHdV = \frac{\mu_0 b_w l_w}{2}\int_0^h H(x)^2 dx = \frac{\mu_0 l_w}{2b_w \sinh^2(\gamma h)}\int_0^h \left[\sum_{k=1}^{n} i_k \sinh(\gamma h) + \sum_{k=1}^{n-1} i_k \sinh(\gamma h - \gamma x)\right]^2 dx$$
$$= \frac{\mu_0 l_w}{8b_w \gamma \sinh^2(\gamma h)} \left\{ \begin{array}{l} \left(\sum_{k=1}^{n} i_k\right)^2 [\sinh(2\gamma h) - 2\gamma h] + \left(\sum_{k=1}^{n-1} i_k\right)^2 [\sinh(2\gamma h) - 2\gamma h] \\ +2\left(\sum_{k=1}^{n-1} i_k\right)\left(\sum_{k=1}^{n} i_k\right)[2\gamma h \cosh(\gamma h) - 2\sinh(\gamma h)] \end{array} \right\} \tag{8}$$

$$E_{lk} = \left\{ \begin{array}{ll} \frac{\mu_0 l_w}{8b_w \gamma \sinh^2(\gamma h)} \left\{ \begin{array}{c} \left(\sum_{k=1}^{n} i_k\right)^2 [\sinh(2\gamma h) - 2\gamma h] \\ +\left(\sum_{k=1}^{n-1} i_k\right)^2 [\sinh(2\gamma h) - 2\gamma h] \\ +2\left(\sum_{k=1}^{n-1} i_k\right)\left(\sum_{k=1}^{n} i_k\right)[2\gamma h \cosh(\gamma h) - 2\sinh(\gamma h)] \end{array} \right\} & k = 2j-1,\ j = 1, 2, 3 \cdots n \\ \frac{\mu_0 l_w w}{2b_w}(i_1 + i_2 + \cdots + i_j)^2 & k = 2j,\ j = 1, 2, 3 \cdots n-1 \end{array} \right. \tag{9}$$

$$E_l = \sum_{k=1}^{2n-1} E_{lk} = \frac{\mu_0 l_w w}{2b_w}[{i_1}^2 + (i_1 + i_2)^2 + \cdots + (i_1 + i_2 + \cdots + i_{n-1})^2]$$
$$+ \frac{\mu_0 l_w}{8b_w \gamma \sinh^2(\gamma h)} \left\{ \begin{array}{l} \left[2{i_1}^2 + 2(i_1+i_2)^2 + \cdots + 2\left(\sum_{k=1}^{n-1} i_k\right)^2 + \left(\sum_{k=1}^{n-1} i_k\right)^2\right][\sinh(2\gamma h) - 2\gamma h] \\ +4\left[i_1(i_1+i_2) + (i_1+i_2)(i_1+i_3) + \cdots + \left(\sum_{k=1}^{n-1} i_k\right)^2 \left(\sum_{k=1}^{n} i_k\right)^2\right][\gamma h \cosh(\gamma h) - \sinh(\gamma h)] \end{array} \right\} \tag{10}$$

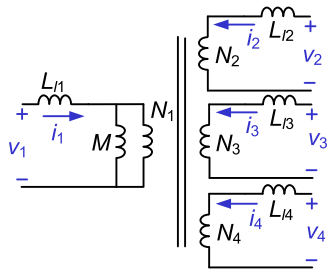

Fig. 7. π-model of the multi-winding planar transformer.

priority of leakage inductance request of each winding and then the optimal winding configuration can be solved.

To introduce the details of this part, a four-winding multiple-output planar transformer is used as an example. According to the method, a limited number of cases that have relatively low leakage magnetic field energy are screened out. Then, the optimal winding configuration in these cases can be found. It is convenient to solve self-inductance and mutual-inductance matrix by modeling the transformer in Maxwell. The relationship between the leakage inductances and inductance matrix is

$$\begin{pmatrix} v_1 \\ v_2 \\ v_3 \\ v_4 \end{pmatrix} = \begin{pmatrix} L_{11} & M_{12} & M_{13} & M_{14} \\ M_{21} & L_{22} & M_{23} & M_{24} \\ M_{31} & M_{32} & L_{33} & M_{34} \\ M_{41} & M_{42} & M_{43} & L_{44} \end{pmatrix} \frac{d}{dt} \begin{pmatrix} i_1 \\ i_2 \\ i_3 \\ i_4 \end{pmatrix}. \tag{11}$$

Fig. 7 shows the π model of a multi-winding planar transformer. N_1, N_2, N_3, and N_4 are the turns of windings. L_{l1}, L_{l2}, L_{l3}, and L_{l4} are the leakage inductances. M is the magnetic inductance.

Once the inductance matrix is obtained, the leakage inductance of each winding in different situations can be calculated. For example, the leakage inductance of the primary winding can be calculated when other windings are shorted. In (12), the relationship of voltage and current in each winding is up to the inductance matrix. Using Laplace transform, the results are simplified. The relationship of i versus v can be calculated by matrix operation. In (14), the matrix G is the inverse of matrix L

$$L = \begin{pmatrix} L_{11} & M_{12} & M_{13} & M_{14} \\ M_{21} & L_{22} & M_{23} & M_{24} \\ M_{31} & M_{32} & L_{33} & M_{34} \\ M_{41} & M_{42} & M_{43} & L_{44} \end{pmatrix} \tag{12}$$

$$v = s \cdot L \cdot i \tag{13}$$

$$G = L^{-1} \tag{14}$$

$$i = \frac{1}{s} \cdot G \cdot v. \tag{15}$$

The elements in matrixes i and v are shown as follows:

$$i = \begin{pmatrix} i_1 & i_2 & i_3 & i_4 \end{pmatrix}^T \tag{16}$$

$$v = \begin{pmatrix} v_1 & v_2 & v_3 & v_4 \end{pmatrix}^T. \tag{17}$$

TABLE II
PLANAR TRANSFORMER LAYERS

	Turns	Layers
Primary	24	6
5 V	3	4
12 V	7	2
-12 V	7	2
Auxiliary	7	2

To find out the leakage inductance, the equivalent voltages of different windings need to be set. For example, the leakage inductance of the primary side can be conveniently obtained by setting $v_2 = v_3 = v_4 = 0$ and $v_1 = 1$. Then, the leakage inductance of the first winding is $1/G_{11}$. In the same way, $1/G_{22}$, $1/G_{33}$, and $1/G_{44}$ are the leakage inductances of other windings

$$\begin{pmatrix} i_1 \\ i_2 \\ i_3 \\ i_4 \end{pmatrix} = \frac{1}{s} \cdot \begin{pmatrix} G_{11} & G_{12} & G_{13} & G_{14} \\ G_{21} & G_{22} & G_{23} & G_{24} \\ G_{31} & G_{32} & G_{33} & G_{34} \\ G_{41} & G_{42} & G_{43} & G_{44} \end{pmatrix} \cdot \begin{pmatrix} v_1 \\ v_2 \\ v_3 \\ v_4 \end{pmatrix}. \tag{18}$$

By comparing the calculated leakage inductance of those structures that are selected from the first step, the structure that has low leakage inductance in 5 V output channel and primary-side circuit can be selected finally.

V. OPTIMIZATION EXAMPLE OF A 1-MHZ THREE-OUTPUT MULTI-WINDING PLANAR TRANSFORMER

A. Design of a Multi-Winding Planar Transformer

Based on the requirement of the multiple-output ACF converter, the parameters of the multiple-output planar transformer are designed here. According to the input and output parameters in Table I, the specifications of the multi-winding planar transformer are given in Table II. Considering the number of windings is large, there are many ports in the planar transformer. In order to arrange the ports of a planar transformer well, the cores with a wide interface area are adopted. By comparing the loss distribution and considering the connection of multilayers, the core size is chosen as EE14. The MnZn soft ferrite material 3F45 from FERROXCUBE is chosen for low power loss and high performance at 1 MHz.

It is noted that the copper thickness is adjusted to the frequency condition in the design process of this multi-winding planar transformers. The general design criterion is that the thickness should be lower than two times the skin depth. Considering the manufacture situation, the thickness of the copper layer in both primary and secondary windings is kept the same.

B. Optimization of the Multi-Winding Planar Transformer

1) Numerical Analysis of Winding Configurations: In this part, a preliminary screening of all the winding configurations will be carried out. As presented in Table II, the total number of layers in the multi-winding planar transformer is 16. By making a full permutation of winding arrangement and removing

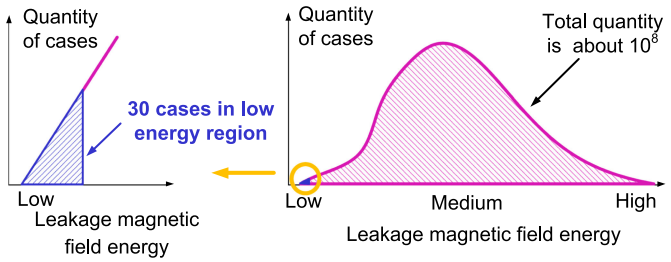

Fig. 8. Quantity distribution of cases with different leakage magnetic field energies.

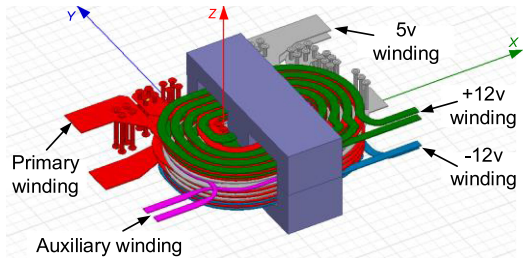

Fig. 9. Three-dimensional model of the multi-winding planar transformer.

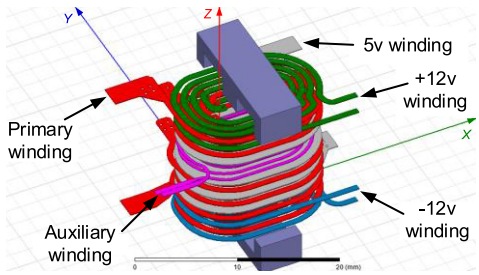

Fig. 10. Splitting windings of the multi-winding planar transformer.

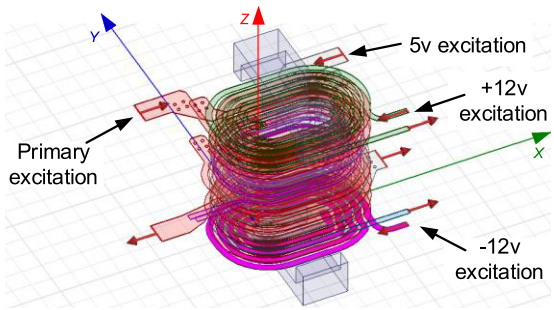

Fig. 11. Current excitations of windings in the planar transformer.

the repeated structures, the total winding configuration is about 1.5×10^8. Among so many structures, most of them have large leakage inductance and are not suitable for the multiple-output converters. So these unsuitable cases should be eliminated.

According to the method proposed in Section III, the primary goal can be achieved in MATLAB. For a certain structure that exists in all cases, the expression of MMF distribution can be listed and then the leakage magnetic field energy that represents the magnitude of the leakage inductance can be calculated.

By traversing all the winding configurations, about 30 cases that have low leakage magnetic field energy can be screened out. In this way, the scale of winding configuration can be exponentially reduced from 1.5×10^8 to about 30. Many inappropriate configurations can be filtered out. These selected cases will be analyzed in the following section. In this selecting procedure, the algorithm is programmed in MATLAB and the basic information of the multiple-output transformer is imported to start the screening process. The turns and currents of each winding, the copper thickness in each layer, and the distance between two layers are loaded into MATLAB. The leakage magnetic field energy of all winding structures is recorded and all the winding structures will be sorted by the leakage magnetic field energy.

Fig. 8 shows the quantity distribution of cases with leakage magnetic field energy and shows the quantity is small in both low and high leakage magnetic field energy region, while in the medium leakage magnetic field energy region, the quantity is large. The shape of a distribution diagram is close to a normal distribution curve. In the low leakage magnetic field energy region, about 30 structures starting from the lowest leakage magnetic energy can be conveniently chosen. It is noted that there might be a winding structure with larger total leakage energy but with less leakage inductance for 5 V winding. However, minimizing the leakage inductance of all windings is our first priority. Based on this, we optimize the leakage inductance of the 5 V output channel.

2) FEA Simulation Analysis of Winding Configuration: The key is how to find the most suitable winding arrangement among the 30 cases selected from the previous analysis. FEA software Maxwell plays an important role in selecting the most suitable winding structure. In Maxwell, the planar transformer needs to be modeled and the simulation frequency should be set correctly. The self-inductance and mutual-inductance matrix can be obtained from the simulation results. One winding configuration can cost about 20 min to simulate. So the total time to complete the 30 cases will cost about 10 h. About 30 cases that have low total leakage magnetic field energy are a reasonable and feasible scale to select the optimal case. The more cases Maxwell simulates, the more time it takes. Compared with original winding structure number 1.5×10^8, the simulation energy and time have been reduced significantly.

Fig. 9 shows the three-dimensional model of the multi-winding planar transformer. There are five windings in this planar transformer. The red winding is the primary winding and the pink one is the auxiliary winding. In the secondary side, the 5 V winding is gray and $\pm$ 12 V windings are green and blue. Fig. 10 shows the splitting windings of the multi-winding planar transformer. The distribution of layers is demonstrated in Fig. 10.

Fig. 11 shows the current excitations of windings in the multi-winding planar transformer. The direction of the current follows the dotted terminal of the planar transformer. During the simulation progress, the detailed mesh plots are illustrated in Fig. 12. It is noted that the Maxwell solver is eddy current solver and the excitation is current.

Fig. 13 shows the optimal winding structure and MMF distribution. The left part is the winding structure and the right part

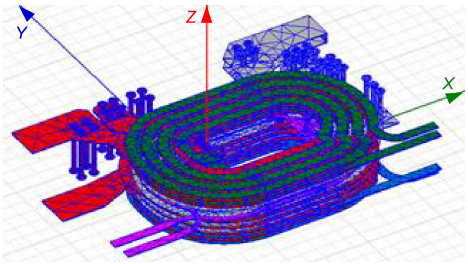

Fig. 12. Detailed mesh plots of windings in the planar transformer.

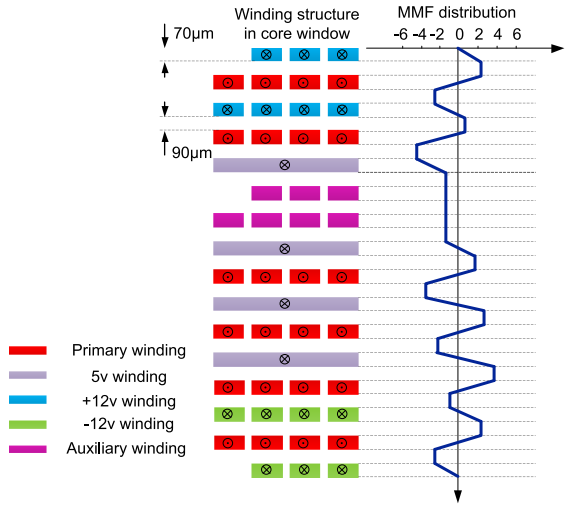

Fig. 13. Optimal winding and MMF distribution.

TABLE III
SIMULATED SELF- AND MUTUAL-INDUCTANCE MATRIX (UNIT: μH)

	N_1	N_3	N_4	N_5
N_1	114.17	33.101	33.351	14.241
N_3	33.101	9.9625	9.4864	4.1093
N_4	33.351	9.4864	10.038	4.1547
N_5	14.241	4.1093	4.1547	1.7956

is the MMF distribution. The copper thickness is selected to be 70 μm (2 oz) and the interlayer spacing is about 90 μm. The current direction in each winding has been pointed out. Since the current in the auxiliary winding is low, the ampere-turns of the auxiliary winding are small compared to other output power windings. So the variation of MMF distribution of the auxiliary winding can be negligible. The curve in the right part is close to the vertical axis. The MMF distribution in Fig. 13 is based on the assumption that the current is distributed evenly through the conductors.

Table III presents the self-inductance and mutual-inductance matrix obtained from the simulation results. N_1 represents the primary winding. N_3, N_4, and N_5 are the windings of the secondary side, in which N_3 and N_4 are the $\pm$ 12 V output windings and N_5 is the +5 V output winding.

It should be emphasized that all windings are added with current excitation in the simulation. And only one simulation is needed to find all leakage inductances. When the self-inductance and mutual-inductance matrix is obtained, the leakage inductance in each winding can be calculated numerically. Using the above-mentioned method, the leakage inductance in each winding can be calculated as given in Table IV. L_{lp} represents the leakage inductance in the primary side, while the secondary side windings are shorted. L_{ls3} represents the leakage inductance in the 5 V output channel, while the primary winding and $\pm$12 V circuit windings are shorted. In the same way, L_{ls1} and L_{ls2} represent the leakage inductance in the $\pm$12 V circuit when other windings are shorted.

TABLE IV
SIMULATED LEAKAGE INDUCTANCE OF EACH WINDING AT 1 MHZ

	L_{lp}	L_{ls1}	L_{ls2}	L_{ls3}
Simulated results	0.51 μH	0.27 μH	0.30 μH	0.018 μH

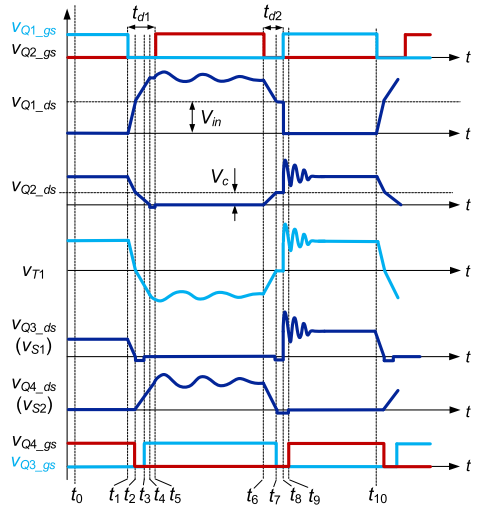

Fig. 14. Key waveforms of the ACF forward multiple-output converter.

The proportion of leakage inductance in the primary side and 5 V output is very small. The percentage of the leakage inductance in the primary side is about 0.5% and the percentage of the leakage inductance in the 5 V output channel is about 1%. It is noted that the optimal winding configuration is chosen in FEA simulation. The structures that realize low leakage inductance in primary side and 5 V output channel can be found.

VI. MODE ANALYSIS AND OSCILLATION MODELING

The key waveforms of the ACF multiple-output converter are shown in Fig. 14. By analyzing the mode equivalent circuits with the parasitic inductance and capacitance, the oscillation frequency and amplitude of oscillation can be derived theoretically. Then, the root reason of oscillation in the power devices can be explained quantitatively.

S_1 and S_2 are two ports of 5 V output winding. V_{S1} is the drain–source voltage of SR Q_3 and is used to drive the SR Q_4. V_{S2} is the drain–source voltage of SR Q_4 and is used to drive SR Q_3. The waveforms of V_{S1} and V_{S2} are also shown in Fig. 14. Operation principle of the ACF multiple-output converter is analyzed in this section. The oscillation frequency and amplitude of switches have been calculated in the analysis process. Fig. 15 shows the equivalent mode analysis.

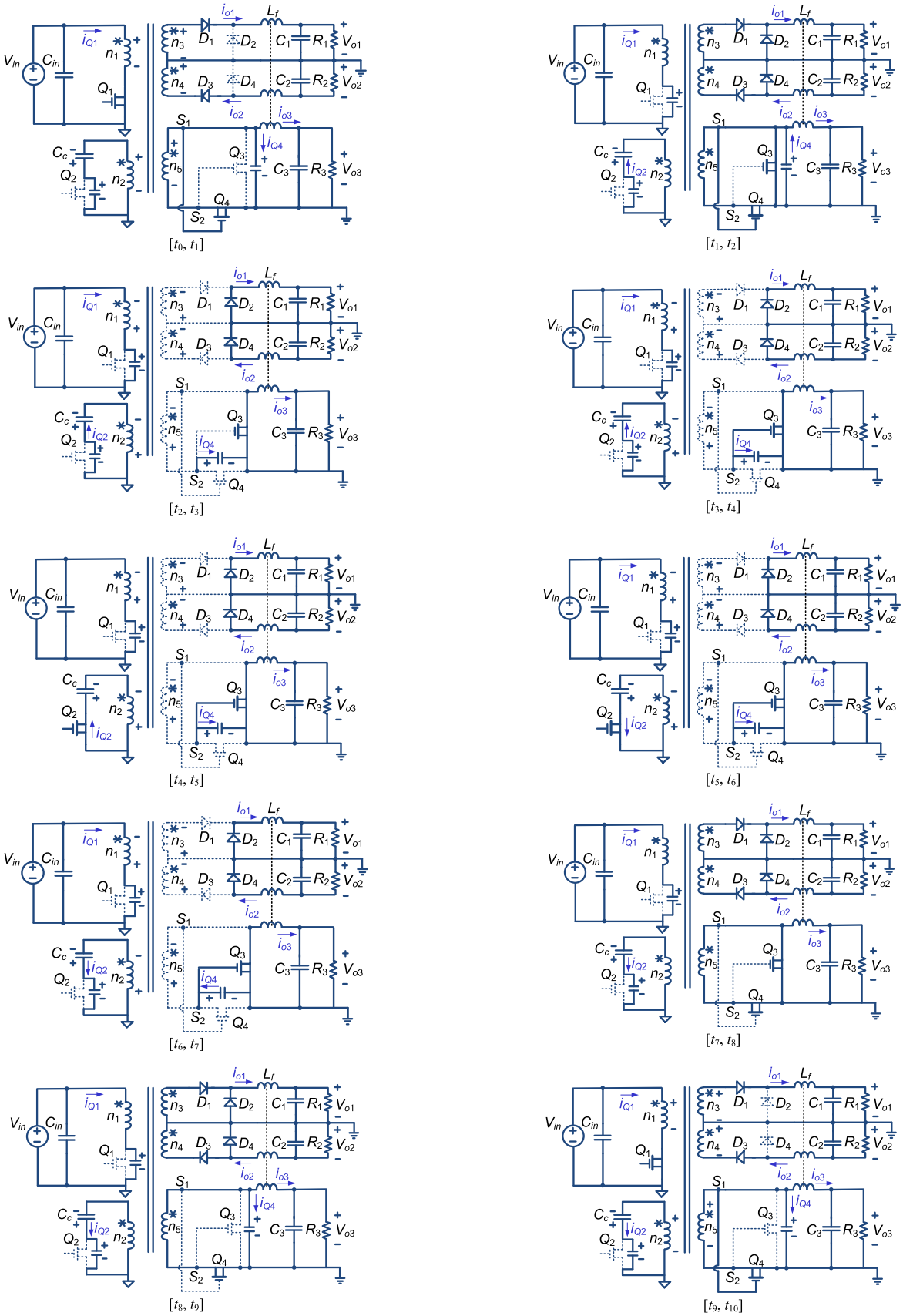

Fig. 15. Equivalent mode analysis.

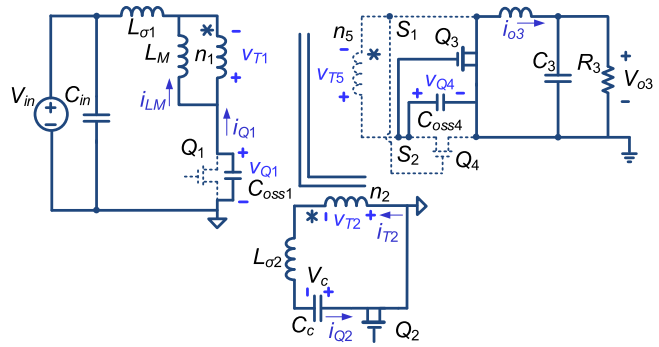

Fig. 16. Equivalent circuit with parasitic parameters: $[t_5,\ t_6]$.

1) Interval 1 $[t_0,\ t_1]$: The control HEMT Q_1 turns ON and the clamping HEMT Q_2 turns OFF in this period. The power transfers from primary side to secondary side. The load current in the secondary side flows through SR Q_4.
2) Interval 2 $[t_1,\ t_2]$: The control HEMT Q_1 turns OFF in this period; the load current is referred to the primary side to charge the junction capacitor of Q_1. At the end of this interval, the voltage v_{Q1_ds} increases to the input voltage V_{in} and the voltage v_{Q2_ds} decreases to the voltage of clamping capacitor V_c. The load current still flows through Q_4. The voltage of SR Q_3 decreases to zero.

According to voltage-second balance within one switching period, the relationship between the input voltage V_{in} and the clamping capacitor voltage V_c is

$$\frac{V_c(1-D)T_s}{n_2} = \frac{V_{\text{in}}DT_s}{n_1}. \tag{19}$$

The clamping capacitor voltage V_c is

$$V_c = \frac{n_2 D}{n_1(1-D)}V_{\text{in}}. \tag{20}$$

3) Interval 3 $[t_2,\ t_3]$: Both the control HEMT Q_1 and clamping HEMT Q_2 turn OFF. v_{Q1_ds} continues to increase and v_{Q2_ds} continues to decrease. The SR Q_4 turns OFF and the voltage of SR Q_4 begins to increase. The load current flows from Q_4 to Q_3. Considering the delay time of the drive chip, there is no drive signal on the SR Q_3 in this interval. The SR Q_3 is reversely conducting.
4) Interval 4 $[t_3,\ t_4]$: The SR Q_3 turns ON. At the end of this interval, v_{Q2_ds} reaches zero and the clamping HEMT Q_2 starts reversely conducting.
5) Interval 5 $[t_4, t_5]$: The clamping HEMT Q_2 is reversely conducting. The clamping capacitor voltage is applied to the transformer winding and the magnetic current starts to decrease. At time t_5, the clamping HEMT turns ON. The load current continues to flow through Q_3.
6) Interval 6 $[t_5,\ t_6]$: The clamping HEMT Q_2 turns ON and the control HEMT Q_1 turns OFF. The core starts to reset. The magnetic current decreases to zero and begins to reverse. At time t_6, the core finishes the reset process. Considering the parasitic parameters, the equivalent circuit of this interval is shown in Fig. 16.

The relationships of voltages and currents are listed as follows:

$$\begin{cases} i_{Q1} = -C_{\text{oss1}} \cdot dv_{Q1}/dt \\ i_{LM} = i_{T1} + i_{Q1} \\ i_{T2} = i_{Q2} \\ i_{T1}/i_{T2} = n_2/n_1 \\ v_{T1} = -V_{\text{in}} + v_{Q1} - L_{\sigma1} \cdot di_{Q1}/dt \\ v_{T2} = V_c - L_{\sigma2} \cdot di_{Q2}/dt \\ v_{T5} = v_{Q4} \\ v_{T1}/v_{T2} = n_1/n_2 \\ v_{T1}/v_{T5} = n_1/n_5. \end{cases} \tag{21}$$

Then, solving (21), the expression of v_{Q1} is

$$v_{Q1}(t) = \frac{V_{\text{in}}DT_s}{2L_M}\sqrt{\frac{(L_{\sigma1} + L_{\sigma2}n_1{}^2/n_2{}^2)}{C_{\text{oss1}}}} \sin\left[\frac{(t-t_4)}{\sqrt{(L_{\sigma1} + L_{\sigma2}n_1{}^2/n_2{}^2)C_{\text{oss1}}}}\right] + V_{\text{in}} + V_c n_1/n_2. \tag{22}$$

The oscillation frequency of v_{Q1} is

$$f_{r\text{-}Q_1} = \frac{1}{2\pi\sqrt{(L_{\sigma1} + L_{\sigma2}n_1{}^2/n_2{}^2)C_{\text{oss1}}}}. \tag{23}$$

The oscillation amplitude of v_{Q1} is

$$A_{r\text{-}Q_1} = \frac{V_{\text{in}}DT_s}{2L_M}\sqrt{\frac{(L_{\sigma1} + L_{\sigma2}n_1{}^2/n_2{}^2)}{C_{\text{oss1}}}}. \tag{24}$$

The voltage of Q_4 is derived as

$$v_{Q4}(t) = \frac{V_{\text{in}}DT_s n_5}{2L_M n_1}\sqrt{\frac{(L_{\sigma1} + L_{\sigma2}n_1{}^2/n_2{}^2)}{C_{\text{oss1}}}} \sin\left[\frac{(t-t_4)}{\sqrt{(L_{\sigma1} + L_{\sigma2}n_1{}^2/n_2{}^2)C_{\text{oss1}}}}\right] + V_c n_5/n_2. \tag{25}$$

The oscillation frequency of v_{Q4} is

$$f_{r\text{-}Q_4} = \frac{1}{2\pi\sqrt{(L_{\sigma1} + L_{\sigma2}n_1{}^2/n_2{}^2)C_{\text{oss1}}}}. \tag{26}$$

The oscillation amplitude of v_{Q4} is

$$A_{r\text{-}Q_4} = \frac{V_{\text{in}}DT_s n_5}{2L_M n_1}\sqrt{\frac{(L_{\sigma1} + L_{\sigma2}n_1{}^2/n_2{}^2)}{C_{\text{oss1}}}}. \tag{27}$$

The oscillation frequency and amplitude are related to $L_{\sigma1}$, $L_{\sigma2}$, and C_{oss1}. Once the magnitude of the leakage inductance is large, the high voltage spike will happen in control HEMT Q_1 and rectifier Q_4. In order to reduce the voltage spike in control HEMT Q_1 and rectifier Q_4, the leakage inductance should be minimized.

7) Interval 7 $[t_6,\ t_7]$: The clamping HEMT Q_2 turns OFF. The magnetizing inductance and the junction capacitance form the resonant circuit. v_{Q1_ds} starts to decrease

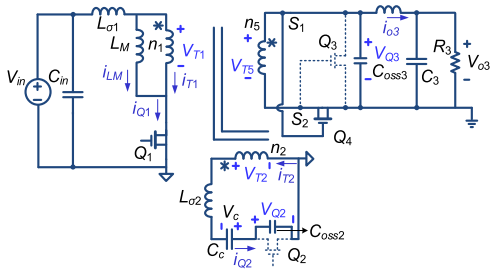

Fig. 17. Equivalent circuit with parasitic parameters: $[t_9, t_{10}]$.

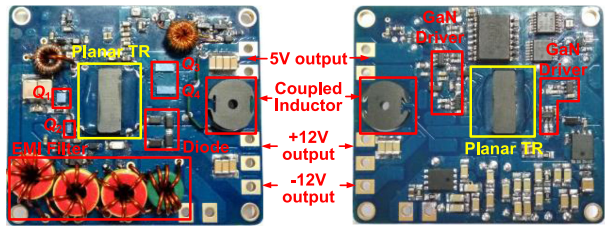

(a) (b)

Fig. 18. Photograph of the prototype. (a) Top. (b) Bottom.

and v_{Q2_ds} starts to increase from zero. At the end of this period, v_{Q1_ds} reaches input voltage V_{in} and v_{Q2_ds} reaches V_c.

8) Interval 8 $[t_7,\ t_8]$: Both the control HEMT Q_1 and clamping HEMT Q_2 turn OFF. The transformer winding voltage is zero. In the secondary-side, both the SRs reversely conduct. Considering Q_3 and Q_4 are eGaN HEMTs, the reverse conduction mechanism results in high reverse conduction voltage that will cause high power loss. This interval should be reduced to minimum.
9) Interval 9 $[t_8,\ t_9]$: Considering the delay time of the drive chip, there is no drive signal on SR Q_4. The SR Q_4 is reversely conducting at this interval. The SR Q_3 turns OFF.
10) Interval 10 $[t_9,\ t_{10}]$: The control HEMT Q_1 turns ON. The transformer begins positive magnetization. The load current flows from Q_3 to Q_4 and Q_3 turns OFF. The voltage of SR Q_3 begins to increase. Considering the leakage inductances in the primary and auxiliary windings, the equivalent circuit with the parasitic parameters is shown in Fig. 17

$$\begin{cases} i_{Q2} = C_{\text{oss2}} \cdot dv_{Q2}/dt \\ i_{Q1} = i_{LM} + i_{T1} \\ i_{T2} = i_{Q2} \\ i_{T1}/i_{T2} = n_2/n_1 \\ v_{T1} = V_{\text{in}} - L_{\sigma1} \cdot di_{Q1}/dt \\ v_{T2} = v_{Q2} - V_c + L_{\sigma2} \cdot di_{Q2}/dt \\ v_{T5} = v_{Q3} \\ v_{T1}/v_{T2} = n_1/n_2 \\ v_{T1}/v_{T5} = n_1/n_5. \end{cases} \tag{28}$$

Then, solving (28), the expression of v_{Q2} is

$$v_{Q2}(t) = \frac{V_{\text{in}} D T_s n_1}{2 L_M n_2} \sqrt{\frac{(L_{\sigma2} + L_{\sigma1} n_2^2/n_1^2)}{C_{\text{oss2}}}} \sin\left[\frac{(t - t_7)}{\sqrt{(L_{\sigma2} + L_{\sigma1} n_2^2/n_1^2) C_{\text{oss2}}}}\right] + V_c + V_{\text{in}} n_2/n_1. \tag{29}$$

Then, the oscillation frequency of v_{Q2} is

$$f_{r\_Q_2} = \frac{1}{2\pi \sqrt{(L_{\sigma2} + L_{\sigma1} n_2^2/n_1^2) C_{\text{oss2}}}}. \tag{30}$$

TABLE V
COMPONENTS IN THE MULTIPLE-OUTPUT CONVERTER

Q_1	EPC2025 (EPC) (300V/4A, eGaN)	n_1:n_2:n_3:n_4:n_5	24:7:7:7:3
Q_2	EPC2012C (EPC) (200V/5A, eGaN)	Diode	PMEG10020ELR (NXP)
Q_3, Q_4	EPC2015C (EPC) (40V/36A, eGaN)	Core	EE14/3.5/5 (3F45)

The oscillation amplitude of v_{Q2} is

$$A_{r\_Q_2} = \frac{V_{\text{in}} D T_s n_1}{2 L_M n_2} \sqrt{\frac{(L_{\sigma2} + L_{\sigma1} n_2^2/n_1^2)}{C_{\text{oss2}}}}. \tag{31}$$

The voltage of Q_3 is derived as

$$v_{Q3}(t) = \frac{V_{\text{in}} D T_s n_5}{2 L_M n_1} \sqrt{\frac{(L_{\sigma2} + L_{\sigma1} n_2^2/n_1^2)}{C_{\text{oss2}}}} \sin\left[\frac{(t - t_7)}{\sqrt{(L_{\sigma2} + L_{\sigma1} n_2^2/n_1^2) C_{\text{oss2}}}}\right] + V_{\text{in}} n_5/n_1. \tag{32}$$

The oscillation frequency of v_{Q3} is

$$f_{r\_Q_3} = \frac{1}{2\pi \sqrt{(L_{\sigma2} + L_{\sigma1} n_2^2/n_1^2) C_{\text{oss2}}}}. \tag{33}$$

The oscillation amplitude of v_{Q3} is

$$A_{r\_Q_3} = \frac{V_{\text{in}} D T_s n_5}{2 L_M n_1} \sqrt{\frac{(L_{\sigma2} + L_{\sigma1} n_2^2/n_1^2)}{C_{\text{oss2}}}}. \tag{34}$$

The oscillation frequency and amplitude are related to $L_{\sigma1}$, $L_{\sigma2}$, and C_{oss2}. Once the magnitude of leakage inductance is large, high voltage spike normally happens over the clamping HEMT Q_2 and rectifier Q_3.

VII. EXPERIMENTAL VERIFICATION AND DISCUSSION

An experimental prototype operating at 1 MHz, 100 V input and 5 V/6 A and ±12 V/0.83 A outputs was built. Fig. 18 shows the photograph of the prototype. The powertrain printed circuit board (PCB) is eight layers. The drive circuits of eGaN HEMTs are placed in the bottom layer of the main PCB board. The yellow rectangle in Fig. 18 is the multi-winding planar transformer with 16 layers. The copper thickness of each layer is selected to be 70 μm (2 oz) and the interlayer distance is about 90 μm. Table V

TABLE VI
MEASURED LEAKAGE INDUCTANCES (UNIT: μH)

	L_{lp}	L_{ls1}	L_{ls2}	L_{ls3}
Simulated results	0.51	0.27	0.30	0.018
Experimental results	0.65	0.35	0.37	0.025

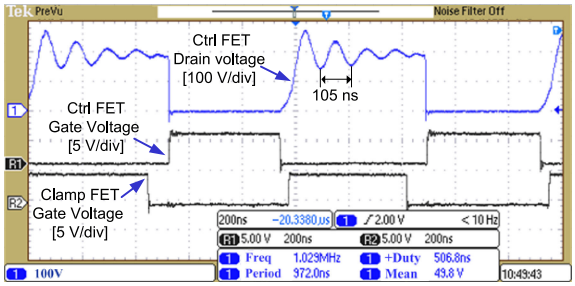

Fig. 19. Waveforms of Q_1: $V_{\text{in}} = 100$ V, $V_{o1} = 5$ V, $I_{o1} = 6$ A, $V_{o2} = +12$ V, $I_{o2} = 0.83$ A, $V_{o3} = -12$ V, $I_{o3} = 0.83$ A, and $f_s = 1$ MHz.

lists the component values and part numbers in the power stage. The power density is 28.5 W/in^3.

Table VI presents the comparison of simulated and measured leakage inductance in each winding. The experimental leakage inductances of each winding are measured with an *LCR* instrument. Measurement condition is that winding is connected to the instrument, while other windings are shorted. In simulated results, compared with the magnetic inductance of the multi-winding planar transformer, the percentage of leakage inductance in the primary side is about 0.5% and the percentage of leakage inductance in the 5 V output channel is about 1%. The corresponding two percentages are about 0.59% and 1.5%. The results match the simulation results well. The leakage inductances in $\pm$12 V outputs are relatively larger compared with the windings of the primary side and 5 V output channel.

The leakage inductance of each winding was measured in the experimental results. Then, the oscillation frequency can be calculated with the junction capacitance from the device datasheets. The output capacitance of Q_1 is 100 pF and the output capacitance of Q_2 is 50 pF. So the calculated oscillation frequency of control HEMT Q_1 is 9 MHz from (22), and the oscillation frequency of clamping HEMT Q_2 is 35 MHz from (29).

The optimization provides the design preference to select the winding structure that has low leakage inductance in primary side and 5 V output channel in the case of low leakage magnetic field energy. Fig. 19 shows the drain and gate voltage waveforms of the control HEMT. It is observed that the drain voltage is approximately rectangle wave with voltage oscillation caused by the leakage inductances and junction capacitance of the control HEMT. The calculated frequency of oscillation is 9 MHz. The oscillation period in Fig. 19 is about 105 ns, which translates into the frequency of 9.5 MHz. This experimental result matches the theoretical analysis. The peak drain voltage is 250 V at 100 V input. The oscillation is acceptable and the voltage stress is within the rated voltage of control HEMT Q_1.

The plateau voltage of v_{Q1} is 185 V. The voltage rating of the control HEMT Q_1 is 300 V. For Q_1, a 50-V voltage margin

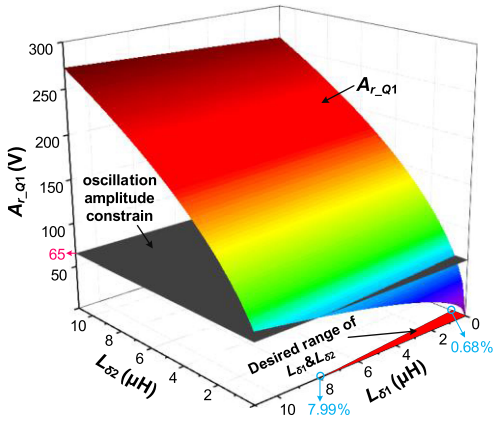

Fig. 20. Desired range of $L_{\delta1}$ and $L_{\delta2}$ for Q_1.

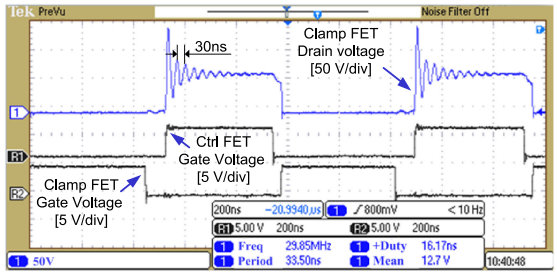

Fig. 21. Waveforms of Q_2: $V_{\text{in}} = 100$ V, $V_{o1} = 5$ V, $I_{o1} = 6$ A, $V_{o2} = +12$ V, $I_{o2} = 0.83$ A, $V_{o3} = -12$ V, $I_{o3} = 0.83$ A, and $f_s = 1$ MHz.

is selected to accommodate extra voltage stress. Hence, the oscillation amplitude of v_{Q1} should be managed below 65 V. Based on (22), the oscillation amplitude of v_{Q1} is only related to $L_{\delta1}$ and $L_{\delta2}$. To manage the voltage spike below Q_1 voltage rating, the leakage inductance should be maintained, as shown in Fig. 20.

Fig. 21 shows the drain and gate voltage waveforms of the clamping HEMT. It is observed that the peak drain voltage of the clamping HEMT is 130 V at 100 V input. With the measured leakage inductances and output capacitance of clamping HEMT Q_2, the calculated oscillation frequency is 35 MHz. The oscillation frequency in Fig. 21 is about 33 MHz, which matches the theoretical analysis. The peak voltage is within the rating voltage of clamping HEMT Q_2.

The plateau voltage of v_{Q2} is 54 V. The voltage rating of the clamping HEMT Q_2 is 200 V. For Q_2, a 50-V voltage margin is selected to accommodate extra voltage stress. Hence, the oscillation amplitude of v_{Q2} should be managed below 96 V. Based on (29), the oscillation amplitude of v_{Q2} is only related to $L_{\delta1}$ and $L_{\delta2}$. To manage the voltage spike below Q_2 voltage rating, the leakage inductance should be maintained, as shown in Fig. 22.

Fig. 23 shows the drain voltage waveforms of the SR HEMTs in the 5 V output channel. The leakage inductance in this channel has been optimized to the minimum. The blue waveform in Fig. 23 is the drain–source voltage of Q_3. The oscillation frequency of the blue waveform is about 9.5 MHz, which corresponds to the oscillation frequency of control HEMT. The red waveform in Fig. 23 is the drain–source voltage of Q_4. The

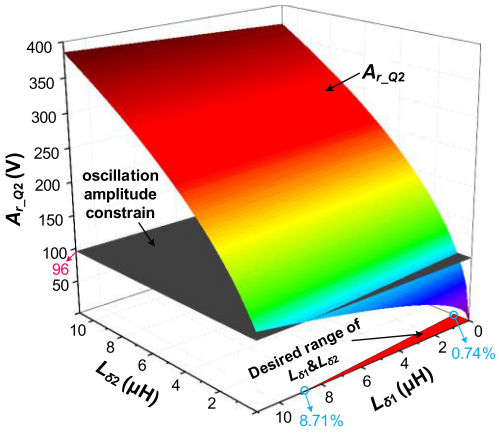

Fig. 22. Desired range of $L_{\delta1}$ and $L_{\delta2}$ for Q_2.

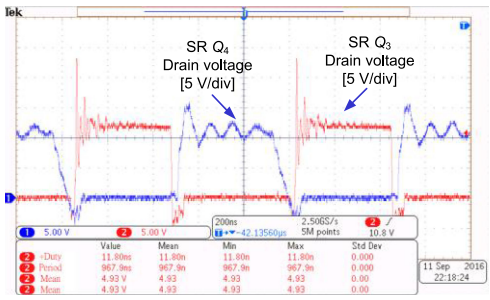

Fig. 23. Waveforms of the SR Q_3 and Q_4: $V_{\text{in}} = 100\,\text{V}$, $V_{o1} = 5\,\text{V}$, $I_{o1} = 6\,\text{A}$, $V_{o2} = +12\,\text{V}$, $I_{o2} = 0.83\,\text{A}$, $V_{o3} = -12\,\text{V}$, $I_{o3} = 0.83\,\text{A}$, and $f_s = 1\,\text{MHz}$.

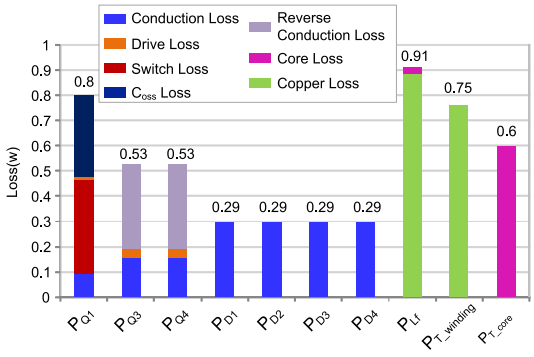

Fig. 24. Theoretical loss distribution of the multi-output forward converter.

oscillation frequency of the blue waveform is about 33 MHz, which corresponds to the oscillation frequency of the clamping HEMT. The peak drain voltage of SR Q_4 is about 23 V and the peak drain voltage of SR Q_3 is about 16 V at 100 V input and full load. The voltage oscillations are within the rated voltage of EPC2015C.

It is noted that in this hard-switching converter, the energy stored in the leakage inductance is not used to achieve the zero-voltage-switching. The leakage inductance is undesirable and should be limited as low as possible.

Fig. 24 shows the converter loss distribution. The condition is under rated input voltage of 100 V and full output load of 50 W.

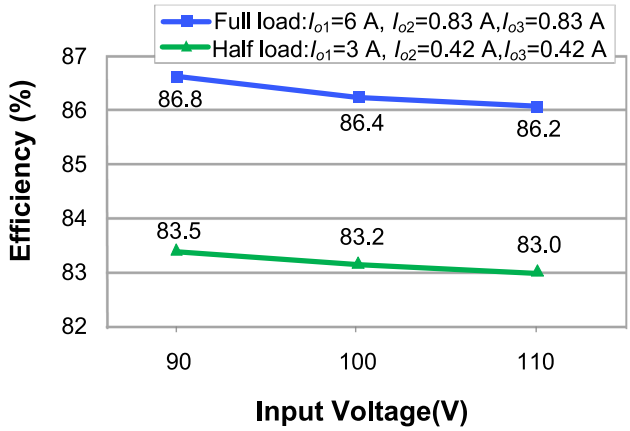

Fig. 25. Efficiency curve at different input voltages: $V_{o1} = 5\,\text{V}$, $V_{o2} = +12\,\text{V}$, $V_{o3} = -12\,\text{V}$, and $f_s = 1\,\text{MHz}$.

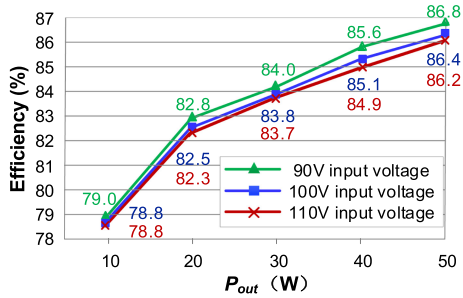

Fig. 26. Efficiency curve at different output powers: $V_{o1} = 5\,\text{V}$, $V_{o2} = +12\,\text{V}$, $V_{o3} = -12\,\text{V}$, and $f_s = 1\,\text{MHz}$.

TABLE VII
MEASURED RESULT OF LOAD REGULATION

	5V Output	+12V Output	-12V Output
10 % Load	4.97 V	12.96 V	13.04 V
100 % Load	4.98 V	12.45 V	12.51 V
Load Regulation	0.2 %	4.1 %	4.3 %

The calculated loss is 7.4 W and the corresponding efficiency is 87.1%.

The efficiency was measured with the optimal multi-winding planar transformer. Fig. 25 shows the efficiency curve in different input voltages. The efficiency is above 86.2% among the input voltage range owing to the low leakage inductance. The efficiency is measured under rated input voltage 100 V including the control loss of the pulsewidth modulation (PWM) controller. The two efficiency curves in Fig. 25 are under full-load condition and half-load condition.

The efficiency curve with different output powers is shown in Fig. 26. The peak efficiency with full load is 86.8%. The result is tested in rating input voltage 100 V and the efficiency includes the PWM controller loss. The measured result matches the theoretical loss analysis well.

Table VII presents the measured result of load regulation. The load regulation is obtained by calculating the voltage variation of the tested channel when the load condition of this channel changed from 10% to 100%, and the other two channels re-

mained under the full-load condition. The load regulation of 5 V output is 0.2%. The load regulation of +12 V output is 4.1% (lower than 5%). The load regulation of –12 V output is 4.4%. Since the 5 V output circuit is the main regulated output, the precision of load regulation in 5 V output is the highest among the three outputs.

VIII. Conclusion

This paper focuses on how to achieve the optimal design of a multiple-winding transformer with the asymmetrical turns and currents of each winding. An optimization method that combines numerical calculation and FEA simulation to screen out optimal suitable configuration is proposed. Compared with simply interleaving primary and secondary windings in two-winding transformers, this method can realize the traversal of all possible configurations by MATLAB and search out the optimal configuration according to the leakage inductance request of windings with different output voltages and powers.

The full GaN ACF converter with self-driven SRs is also presented. Compared with the conventional self-driven method, the GaN drive chip for high reliable gate voltage is combined with a self-driven scheme to drive the SR GaN HEMTs. It is noted that the proposed active clamp technology is using the auxiliary winding with the nonfloating GaN switch compared to the conventional high-side clamping circuit, which is important for the satellite applications. The mode equivalent circuits are analyzed here as well in details with the optimal design transformer and devices parasitics. The frequency and amplitude of oscillation in the switches are derived quantitatively. The results show the leakage inductances in the primary winding and main output channel with high current should be minimized as first priority. An experimental prototype was built to verify the proposed method. The measured leakage inductance matches the simulated result well and is only as low as 0.5% of the magnetic inductance. The optimized efficiency with full load is more than 86.2% within the input voltage range. The power density is 28.5 W/ in^3. The proposed method provides an HF and high-efficiency GaN solution for the satellite applications.

References

[1] X. Zhang, L. Xu, Z. Zheng, and Y. Li, "A novel satellite power supply design with multi-winding high frequency transformer," in *Proc. Eur. Conf. Power Electron. Appl.*, 2015, pp. 1–8.

[2] Y. Yang, M. Xu, D. Wang, and Y. Wang, "Towards energy-efficient routing in satellite networks," *IEEE J. Sel. Areas Commun.*, vol. 34, no. 12, pp. 3869–3886, Dec. 2016.

[3] D. C. Bomberger, D. Feldman, D. E. Trucksess, S. J. Brolin, and P. W. Ussery, "The spacecraft power supply system," *Bell Syst. Tech. J.*, vol. 42, no. 4, pp. 943–972, Jul. 1963.

[4] O. Deblecker, C. Versèle, Z. De Grève, and J. Lobry, "Multiobjective optimization of a power supply for space application using a flexible CAD tool," in *Proc. Eur. Conf. Power Electron. Appl.*, 2013, pp. 1–10.

[5] Q. Tong and D. Zhang, "Research on a high output current dc/dc converter with wide input voltage range for space applications," in *Proc. Int. Conf. Integr. Circuits Microsyst.*, 2016, pp. 205–209.

[6] E. Maset, A. Ferreres, J. B. Ejea, E. Sanchis-Kilders, J. Jordan, and V. Esteve, "5kW weinberg converter for battery discharging in high-power communication satellites," in *Proc. IEEE Power Electron. Spec. Conf.*, 2005, pp. 69–75.

[7] M. Cho, "Modeling of secondary arc conditions on satellite solar array," in *Proc. Int. Symp. Discharges Electr. Insul. Vacuum*, 2006, pp. 726–729.

[8] E. Maset *et al.*, "New power conditioning system for battery-free satellite buses with maximum power point tracking," in *Proc. IEEE Appl. Power Electron. Conf.*, 2007, pp. 1299–1305.

[9] P. Jang and B. H. Cho, "Two-switch forward converter with reset winding and an auxiliary active-clamp circuit for a wide input voltage range," *IEEE Trans. Power Electron.*, vol. 32, no. 6, pp. 4491–4502, Jun. 2017.

[10] F. D. Tan, "The forward converter: From the classic to the contemporary," in *Proc. IEEE Appl. Power Electron. Conf.*, 2002, vol. 2, pp. 857–863.

[11] J. Y. Lin, P. J. Liu, and C. Y. Yang, "A dual-transformer active-clamp forward converter with nonlinear conversion ratio," *IEEE Trans. Power Electron.*, vol. 31, no. 6, pp. 4353–4361, Jun. 2016.

[12] M. M. Jovanovic, M. T. Zhang, and F. C. Lee, "Evaluation of synchronous-rectification efficiency improvement limits in forward converters," *IEEE Trans. Ind. Electron.*, vol. 42, no. 4, pp. 387–395, Aug. 1995.

[13] D. J. Perreault *et al.*, "Opportunities and challenges in very high frequency power conversion," in *Proc. IEEE Appl. Power Electron. Conf.*, 2009, pp. 1–14.

[14] S. L. Colino and R. A. Beach, "Fundamentals of gallium nitride power transistors," EPC Co., El Segundo, CA, USA, Appl. Note, 2010.

[15] Z. Zhang, X. W. Zou, Z. Dong, Y. Zhou, and X. Ren, "A 10-MHz eGaN isolated class-Φ_2 DCX," *IEEE Trans. Power Electron.*, vol. 32, no. 3, pp. 2029–2040, Mar. 2017.

[16] Z. Zhang, J. Y. Lin, Y. Zhou, and X. Ren, "Analysis and decoupling design of a 30 MHz resonant SEPIC converter," *IEEE Trans. Power Electron.*, vol. 31, no. 6, pp. 4536–4548, Jun. 2016.

[17] Z. Zhang, Z. Dong, D. D. Hu, X. W. Zou, and X. Ren, "Three-level gate drivers for eGaN HEMTs in resonant SEPIC converters," *IEEE Trans. Power Electron.*, vol. 32, no. 7, pp. 5527–5538, Jul. 2017.

[18] Z. Ouyang and M. A. E. Andersen, "Overview of planar magnetic technology fundamental properties," *IEEE Trans. Power Electron.*, vol. 29, no. 9, pp. 4888–4900, Sep. 2014.

[19] M. A. Saket, N. Shafiei, M. Ordonez, M. Craciun, and C. Botting, "Low parasitics planar transformer for LLC resonant battery chargers," in *Proc. IEEE Appl. Power Electron. Conf. Expo.*, Mar. 2016, vol. 1, pp. 854–858.

[20] M. A. Saket, N. Shafiei, and M. Ordonez, "Planar transformer winding technique for reduced capacitance in LLC power converters," in *Proc. Energy Convers. Congr. Expo.*, Sep. 2016, pp. 1–6.

[21] C. Qing *et al.*, "A new model for multiple-winding transformer," in *Proc. Power Electron. Spec. Conf.*, 1994, vol. 2, pp. 864–871.

[22] C. P. Schultz, "The coupled leakage model of a multiple winding transformer," in *Proc. IEEE Southeastcon*, Nashville, TN, USA, 2011, pp. 6–11.

[23] M. A. Saket, N. Shafiei, and M. Ordonez, "LLC converters with planar transformers: Issues and mitigation," *IEEE Trans. Power Electron.*, vol. 32, no. 6, pp. 4524–4542, Jun. 2017.

[24] Z. Ouyang, O. C. Thomsen, and M. A. E. Andersen, "Optimal design and tradeoff analysis of planar transformer in high-power dc–dc converters," *IEEE Trans. Ind. Electron.*, vol. 59, no. 7, pp. 2800–2810, Jul. 2012.

[25] L. A. R. Tria, D. Zhang, and J. E. Fletcher, "High-frequency planar transformer parameter estimation," *IEEE Trans. Magn.*, vol. 51, no. 11, Nov. 2015, Art. no. 8402604.

[26] J. H. Jung and S. Ahmed, "Flyback converter with novel active clamp control and secondary side post regulator for low standby power consumption under high-efficiency operation," *IET Power Electon.*, vol. 4, no. 9, pp. 1058–1067, Nov. 2011.

[27] J. Z hang, Z. Ouyang, M. C. Duffy, M. A. E. Andersen, and W. G. Hurley, "Leakage inductance calculation for planar transformers with a magnetic shunt," *IEEE Trans. Ind. Appl.*, vol. 50, no. 6, pp. 4107–4112, Nov./Dec. 2014.

[28] S. M. Djuric and G. M. Stojanovic, "A compact planar transformer with an improved winding configuration," *IEEE Trans. Magn.*, vol. 50, no. 11, Nov. 2014, Art. no. 8402204.

[29] S. Stegen and J. Lu, "Structure comparison of high-frequency planar power integrated magnetic circuits," *IEEE Trans. Magn.*, vol. 47, no. 10, pp. 4425–4428, Oct. 2011.

[30] C. Ropoteanu, P. Svasta, and I. Busu, "High-frequency power loss investigation of a planar ferrite core transformer," in *Proc. IEEE 21st Int. Symp. Des. Technol. Electron. Packag.*, Oct. 2015, pp. 61–64.

[31] Z. Ouyang, J. Zhang, and W. G. Hurley, "Calculation of leakage inductance for high-frequency transformers," *IEEE Trans. Power Electron.*, vol. 30, no. 10, pp. 5769–5775, Oct. 2015.

Zhiliang Zhang (S'03–M'09–SM'14) received the B.Sc. and M.Sc. degrees from the Nanjing University of Aeronautics and Astronautics (NUAA), Nanjing, China, in 2002 and 2005, respectively, and the Ph.D. degree from Queen's University, Kingston, ON, Canada, in 2009.

From June to September 2007, he was a Design Engineering Intern with the Burlington Design Center, Linear Technology Corporation. He is currently a Professor with the Aero-Power Sci-Tech Center, NUAA. He authored or coauthored 37 papers in the IEEE TRANSACTIONS ON POWER ELECTRONICS, and more than 70 papers in IEEE conferences. He holds 12 China patents and one U.S. patent. He coauthored the book *High Frequency* MOSFET *Gate Drivers: Technologies and Applications* (IET, 2017). His research interests include high-frequency power conversion with wide bandgap devices.

Dr. Zhang was a Winner of "United Technologies Corporation Rong Hong Endowment" in 1999. He was a recipient of the National Excellent Youth Fund from National Natural Science Foundation of China in 2017. He was a Secretary of the IEEE Power Electronics Society Technical Committee on Power and Control Core Technologies from 2013 to 2016. He is serving as an Associate Editor for the IEEE JOURNAL OF EMERGING AND SELECTED TOPICS OF POWER ELECTRONICS (IEEE JESTPE) from July 2018. He was a Guest Associate Editor for special issue of JESTPE: Resonant and Soft-Switching Techniques With Wide Bandgap Devices in 2018.

Binghui He received the B.S. degree in electrical engineering from Hunan University, Changsha, China, in 2016. He is currently working toward the M.S. degree at the Aero-Power Sci-Tech Center, Nanjing University of Aeronautics and Astronautics, Nanjing, China.

His research interests include GaN dc–dc converters and electromagnetic interference.

Dong-Dong Hu received the B.S. and M.S. degrees in electrical engineering from the Nanjing University of Aeronautics and Astronautics, Nanjing, China, in 2015 and 2018, respectively.

He is currently working as an Electrical Engineer with NARI Technology Development Co., Ltd., Nanjing, China. His research interests include high-frequency GaN applications for power electronic circuits and dc–dc converters.

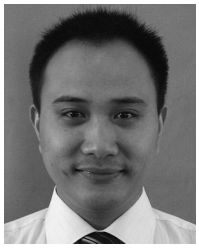

Xiaoyong Ren (S'04–M'11) received the B.S., M.S., and Ph.D. degrees in electrical engineering from the Nanjing University of Aeronautics and Astronautics (NUAA), Nanjing, China, in 2002, 2005, and 2008, respectively.

From 2009 to 2011, he was a Postdoctoral Researcher with the Center for Power Electronics Systems, Virginia Polytechnic Institute and State University, Blacksburg, VA, USA. He is currently with the Department of Electrical Engineering, NUAA. He has authored and coauthored more than ten technical papers published in international journals and conference proceedings. His current research interests include dc–dc conversion, converter control techniques, GaN device applications, and renewable power systems.

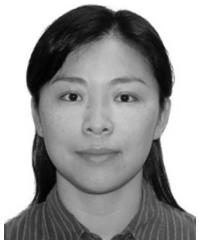

Qianhong Chen (M'06) received the B.S., M.S., and Ph.D. degrees in electrical engineering from the Nanjing University of Aeronautics and Astronautics (NUAA), Nanjing, China, in 1995, 1998, and 2001, respectively.

She is currently a Professor with the Aero-Power Sci-Tech Center. From April 2007 to January 2008, she was a Research Associate with the Department of Electronic and Information Engineering, Hong Kong Polytechnic University, Hung Hom, Hong Kong. She is the Director of the Zhongxing Telecommunication Equipment (NUAA) Joint Laboratory of the communication wireless power transmission technology and one of the main sponsors of the high-power wireless transmission industry alliance in China. Her research interest focuses on the application of integrated-magnetics and wireless power transfer.